Chapter 9
GNSS Remote Sensing of the Environment

GNSS data provide the opportunity to observe Earth system processes with greater accuracy and detail, as they occur.
W.C. Hammond et al. [1]

9.1 Introductory Remarks

GNSS satellites such as GPS are playing an increasingly crucial role in tracking low earth orbiting (LEO) remote sensing satellites at altitudes below 3000 km with accuracies of better than 10 cm [2]. These remote sensing satellites employ a precise global network of GNSS ground receivers operating in concert with receivers onboard the LEO satellites, with all estimating the satellites' orbits, GPS orbits, and selected ground locations simultaneously [2]. In this chapter, we illustrate the role played by GNSS satellites in measuring changes in the Earth's atmosphere, its gravity field, and mass redistribution (e.g., changes in terrestrial water storage). These changes are found by measuring *refractivity* and *inter-satellite distances*.

The last two decades has seen the emergence of GNSS remote sensing techniques that are capable of monitoring changes in the global tropopause height and in so doing, contribute to monitoring *global warming* as we shall see in Chap. 11. GNSS satellites in conjunction, with LEO satellites, e.g., the GRACE (Gravity Recovery And Climate Experiment), have been used to derive vertical atmospheric profiles of, e.g., *temperature*, *height*, and *pressure*, in what is known as GNSS radio occultation (RO) or GNSS-Meteorology [3]. Foelsche et al. [4] point to its potential to overcome problems associated with traditional data sources (e.g., radiosondes) due to their unique combination of *high accuracy* and *vertical resolution*, *long-term stability* and *all-weather global coverage* that is not feasible with other systems.

Indeed, Schmidt et al. [5] compared RO data from CHAMP (CHAllenging Mini-satellite Payload) with radiosonde measurements and found an agreement within less than 0.5 K (i.e., in the measured temperature profiles). In another study of global tropopause height changes over a period of 7 years (2001–2007) using CHAMP and

J. Awange, *GNSS Environmental Sensing*, Environmental Science and Engineering, DOI 10.1007/978-3-319-58418-8_9

GRACE, Schmidt et al. [6], found a trend of +(23–44) m/decade, which is consistent with the results published by [7] based on radiosonde data. The six operational COSMIC (Constellation Observing System for Meteorology, Ionosphere, and Climate) satellites, launched in 2006, have significantly increased the availability of GNSS-RO data for climate studies, see e.g., Anthes et al. [8].

In the next section, a brief look at the basics of GNSS remote sensing of the atmosphere is presented. In Chap. 11, it will be demonstrated how it could be used to enhance tropopause monitoring and in doing so, contribute towards monitoring climatic change. Chapters 11 and 12 will further look at its applicability to climate variability studies. In Sect. 9.2, GNSS remote sensing of the atmosphere for weather forecasting and climatic modelling is presented. Section 9.3 then presents GNSS applications for supporting LEO satellite remote sensing of variations to the gravity field caused by mass changes. The other GNSS remote sensing application of altimetry, which makes use of the measurement of the delay time between the signals that reach the LEO satellite receiver directly from the GNSS transmitter and those that are reflected, e.g., by the sea surface, will be treated in Sect. 9.4.

9.2 GNSS Remote Sensing of the Atmosphere

As stated in part I of the book, some GNSS satellites, such as GPS and GLONASS, were primarily designed to be used by the military with the primary objective of obtaining accurate *positions* of points on the Earth from space. In order to obtain these positions, we saw that the signals emitted by GNSS satellites have to traverse the ionosphere and neutral atmosphere to be received by ground-based GNSS receivers. One of the major obstacles to positioning with GNSS discussed in Sect. 3.4.3 was the *signal delay* caused by atmospheric refraction.

As opposed to geodesists whose interest is to estimate *ionospheric* and *tropospheric* delays only to eliminate them to obtain accurate positions, *meteorologists* and *environmentalists* use these ionospheric and tropospheric delays for *weather forecasting*, *climate studies* (e.g., sea, land, and ice level changes), *hazard predictions* and *early warning systems* (see e.g., Fig. 17.13 on p. 373). Belvis et al. [9] presents a win-win situation for professionals in both geodesy and environmental studies; for a geodesist, accurate knowledge of the atmospheric delay will improve the vertical accuracy, which in turn is of great interest to environmental scientists studying *global climate change*, which may be reflected in changes in the atmospheric delay. Or to put it another way, "one scientist's noise is another scientist's signal".

Currently, the NASA Deep Space Network (DSN) uses near-real-time tropospheric delay estimates based on real-time global differential GNSS (GDGPS discussed in Sect. 5.4.3) to calibrate the radio signals from spacecraft in support of deep space navigation. Real-time global ionospheric total electron content (TEC) maps are derived at JPL and by the Air Force Weather Agency (AFWA) based on

GDGPS tracking data.[1] Hammond et al. [10] point out that GNSS measurements have the potential to contribute to tropospheric weather and climatic modelling, and/or weather forecasting in up to four different ways; (i) integrative measurement of atmospheric water vapor in GPS signal delays, (ii) localized sensing of soil moisture and snow depth from satellite to antenna multipaths, (iii) large-scale sensing of water mass from elastic deformation signals, and (iv) imaging of hydrometeor scattering.

For the ionosphere, where almost all aspects of ionospheric research uses GNSS observations (i.e., the measured *total electronic content* (TEC) from the differential delay of the two L1 and L2 signals), higher sampling rates of real-time GNSS will benefit studies of travelling ionospheric disturbances and other wave phenomena, including disturbances from *earthquakes* and *tsunamis*, while lower latency will aid in the development of operational forecasting for space weather, with significant implications for global communications systems and satellite maintenance [1].

This section examines how GNSS satellites could be used to remote sense various atmospheric parameters as their signals pass through the different portions of the atmosphere. The goal is to show how atmospheric parameters such as the TEC and electron density profile in the ionosphere, tropospheric *temperatures*, *pressures* and *water vapour* could be measured by GNSS satellites, and related to meteorological (weather and climatological) applications, and hence to develop the field of *GNSS-meteorology*. In what follows, we start by presenting the background to GNSS-meteorology before discussing the environmental parameters that could be derived from it. The measuring techniques and the potential applications to environmental monitoring are also discussed.

9.2.1 Background to GNSS-Meteorology

Melbourne [11] suggested that the complicating effect of the atmosphere on GNSS signals could be inverted to remote sense the atmosphere using space-borne techniques. He proposed that LEO satellites be fitted with GNSS receivers and be used to track the signals of rising or setting GNSS satellites (occulting satellites).

The proposed technology is currently playing a major role in complementing existing techniques, e.g., radiosondes. Atmospheric profiles from GNSS remote sensing have been tested in numerical weather prediction (NWP) models and the results were found to be promising [13]. Indeed, Kuo et al. [14] demonstrated using GPS/MET (GPS/meteorology space trial mission) data that the accuracy of global and regional analysis of weather prediction could be significantly improved. Also encouraging were the results of Steiner et al. [15] who showed that highly accurate measurements and fine vertical resolution around the tropopause would be employed to monitor climatic change over the next decades.

[1] http://www.gdgps.net/applications/index.html.

Several atmospheric sounding missions have been launched aboard LEO satellites, e.g., CHAMP, which is no longer active, but whose data are available, GRACE, and COSMIC [8]. The latest entry is the European owned EUropean organization for the exploitation of METeorological SATellites (EUMETSAT), which is installed with a GNSS occultation receivers GRAS (GNSS Receiver for Atmospheric Sounding). Combined, these missions provide more than 5000 occultation data daily. Future possibilities for atmospheric sounding missions may have satellites the size of a laptop with GNSS receivers the size of a credit card, see e.g., Yunck [16]. The planned LEO satellite missions, together with the increasing number of GNSS satellites, promises a bright future for atmospheric studies, which would in turn benefit environmental monitoring. Indeed, such atmospheric sounding missions promise to provide daily global coverage of thousands of remotely sensed data that will be vital for weather, climatic and atmospheric studies.

Space-borne GNSS-meteorology, which we discuss in detail in Sect. 9.2.3.1 is just one part of this new technique. The other component is the ground-based GNSS-meteorology, which will be discussed in Sect. 9.2.3.3. Overviews of this new technique have been presented, for instance, in [17, 18]. In ground-based GNSS-meteorology, a dense GNSS network (e.g., GEONET, Fig. 5.14 on p. 85) is used to measure precisely GNSS path delays caused by the ionosphere and the neutral troposphere traversed by the GNSS signals. These path delays are then converted into TEC and integrated precipitable water vapour (IPWV) values. Conversion to IPWV requires prior information of surface pressure or estimates along the GNSS ray path. These create a continuous, accurate, all weather, real-time lower and upper atmospheric data set with a variety of opportunities for atmospheric research [19].

Use of the GNSS-derived atmospheric precipitate water vapour (PWV) in real-time weather forecasting has, however, been slow due to the fact that forecasters preferred high-rate and low-latency measurements. However, increased availability of high-rate sampling and low-latency GNSS products, e.g., those discussed in Sect. 5.4.3, together with greater station densities, is posed to change the forecasters' perception and lead towards future GNSS water vapor sensing using high-rate, low-latency data from GNSS receivers [10].

9.2.2 GNSS-Derived Atmospheric Parameters

What exactly are the parameters in the atmosphere measurable by GNSS that are of interest to environmental monitoring?

This section attempts to answer this question by examining the effect of the atmosphere on the GNSS signals as they pass through it from the satellites to the receivers. Understanding these effects would in turn enable us know exactly the parameters that could be remotely sensed by GNSS signals. The key to understanding the atmospheric signals of interest is to look at the GNSS signal delays.

The atmosphere acts as a medium through which the GNSS signals travel from the satellites to the receivers. If the atmosphere was a vacuum, the GNSS signal would travel in a straight line. But since the atmosphere is made up of various layers of different densities, the GNSS signal instead curves before reaching the receiver. Hence, the distance increases and the velocity of the radiowaves decreases, thus delaying the signal. In 1992, when GPS attained full operational capability, Ware [20] suggested the possibility of using its delayed signals to remotely sense the atmosphere in what is known as GPS atmospheric sounding. By 1996, the potential of using GPS satellites for atmospheric sounding were already recognised as reported, e.g., by Businger et al., [21, 22]. This GNSS signal delay is what is measured, as will be discussed in the next section. Once the delay has been measured, it is converted into the required atmospheric parameters; *refractivity*, *bending angles*, *temperatures*, *pressures*, *water vapour* and *geopotential heights*. In measuring these atmospheric signals, GNSS-meteorology has the advantages of;

(a) being *global, highly precise and continuous*,
(b) *stable*, owing to the stable GNSS oscillators, and
(c) use of radio frequencies (microwave L-band signals) that can *penetrate* clouds and dust, unlike other remote sensing techniques such as radar-based whose signals are blocked by clouds.

Next, the relationship between the GNSS signals and refractivity as it traverses the troposphere from an altitude of 40 km to the antenna is presented. This will enhance our understanding of how GNSS satellites remotely sense these environmental attributes. Belvis et al. [9] classify the effects of the atmosphere on GNSS signal into two parts:

- *First*, there is a reduction in the speed of propagation of the GNSS signals in a region of finite density compared to that in a vacuum, leading to an increase in the time taken by the signal to reach the receiver. This increase in time can be expressed in terms of *excess path length*, leading to an *optical delay*.
- *Second*, the signals travel in a curved path instead of a straight line due to the refractive effects of the atmosphere's changing density (Snell's laws) (see, Fig. 9.2) leading to a *geometrical delay*.

Both the *optical* and *geometrical delays* are attributed to variations in the *index of refraction n* along the path taken by the signals. The excess path length ΔL is given by [9]

$$\Delta L = \int_L n(s)ds - G, \tag{9.1}$$

where $n(s)$ is the refractive index as a function of position s along the curved path L, and G is the straight-line geometrical path length through the atmosphere (i.e., the path that would be taken by the signal in a vacuum). Equation (9.1) can be expressed as

$$\Delta L = \int_L [n(s) - 1]ds - [S - G], \tag{9.2}$$

where S is the path length along L. In Eq. (9.2), $\int_L [n(s) - 1]ds$ represents the reduction in speed, i.e., optic delay while $[S - G]$ is due to the bending effect, i.e., geometric delay. The bending term $[S - G]$ is smaller, about 1 cm or less, for paths with elevations greater than about 15° [9]. In addition, rather than the refractive index in n above, which is numerically close to unity, refractivity, given by

$$N = (n - 1)10^6 \tag{9.3}$$

is usually used, leading to

$$\boxed{N = 77.6\frac{P}{T} + \left(3.73 \times 10^5 \frac{P_w}{T^2}\right) - \left(40.3 \times 10^6 \frac{n_e}{f^2}\right) + 1.4w}, \tag{9.4}$$

where P denotes the total atmospheric pressure in {mbar}, T is the atmospheric temperature in K, P_w is the partial pressure of water vapour in {mbar}, n_e is the number of electron density per cubic meter {number of electron/m^3}, f is the transmitter frequency in Hz, and w is the liquid water content in g/m^3. The three main contributors to *refractivity*, as was discussed in Sect. 3.4.3, are:

- The *dry neutral atmosphere* (called the hydrostatic component, i.e., the first component on the right-hand-side of Eq. (9.4), dependent mainly on *dry air* and also the *non-dipole component of water vapour*). From this component, GNSS-derived vertical profiles of temperatures and pressures used for global warming monitoring are obtained.
- *Water vapour* (also called the wet or moist component, i.e., the second component on the right-hand-side of Eq. (9.4), dependent on the *dipole component of water vapour*). GNSS are used to measure water vapour through the estimated zenith wet delay (ZWD) as discussed below. The GNSS-derived water vapour are useful both for weather forecasting in numerical weather prediction (NWP) models and also in climate change studies.
- The *free electrons* in the ionosphere (i.e., the third component on the right-hand-side of Eq. (9.4)). GNSS plays a key role in providing slant TEC[2] derived through the differencing of the L1 and L2 frequency phase delay. GPS estimates of slant TEC are by far the most plentiful observations of ionospheric processes and provide the bulk of global spatial sampling, so global models necessarily rely on them heavily [10]. Furthermore, both space-borne and ground-based GPS observations provide information related to various activities and states in the atmosphere, e.g., solar flare and geomagnetic storm [23].

[2]Total electronic contents.

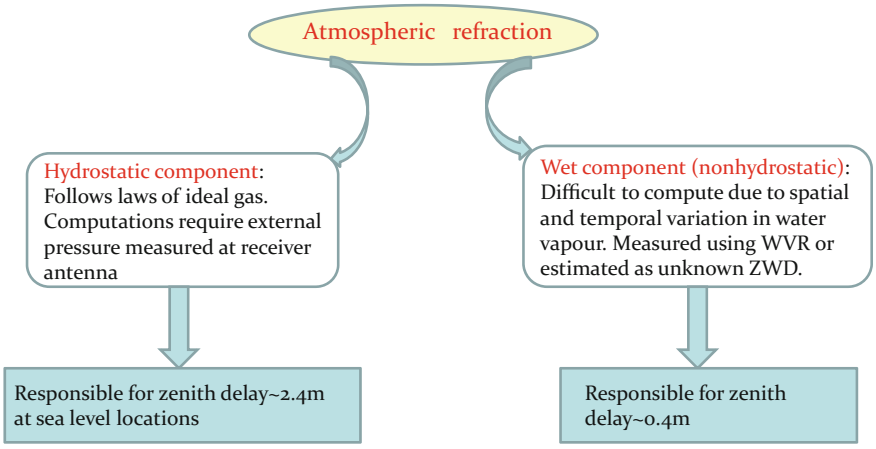

Fig. 9.1 Components of tropospheric refractivity. WVR (water vapour radiometers) and ZWD (zenith wet delay) help in determining the wet component

GNSS Measurement of Water Vapour

The first two items of Eq. (9.4) are summarized in Fig. 9.1. The contribution of the *free electrons* leading to refraction effects on the signals in the ionosphere are corrected for using signals at two frequencies for which these effects are substantially different, taking advantage of the dispersive nature of the ionosphere. This leaves the last term of Eq. (9.4), which is normally very small and is often neglected, see e.g., [9]. The first two terms of Eq. (9.4) are indicated by Resch [24] to be accurate to about 0.5% under normal atmospheric conditions. Thayer [25] provided an improved version [9] of Eq. (9.4), expressed as [26, p. 195]

$$N = k_1 \frac{P_d}{T} Z_d^{-1} + k_2 \frac{P_{wv}}{T} Z_{wv}^{-1} + k_3 \frac{P_{wv}}{T^2} Z_{wv}^{-1}, \tag{9.5}$$

where

- $k_1 = (77.60)\,\mathrm{K\,mbar^{-1}}$, $k_2 = (69.5)\,\mathrm{K\,mbar^{-1}}$, $k_3 = (370100)\,\mathrm{K^2\,mbar^{-1}}$,
- P_d is the *partial pressure of dry air* (in mbar), with the dry gases of the atmosphere in decreasing percentage of volume being $N_2, O_2, Ar, CO_2, Ne, He, Kr, Xe, CH_4, H_2,$ *and* N_2O, representing 99.96% of the total volume,
- P_{wv} is the partial pressure of water vapour (water vapour content is highly variable, but rarely exceeds 1% of the mass of the atmosphere),
- T is the absolute temperature in degrees Kelvin (K),
- Z_d^{-1} and Z_{wv}^{-1} are the *inverse compressibility factors* for dry air and water vapor, respectively, that account for small departures in the behaviour of moist atmosphere from an ideal gas.

Thayer's [25] modified Eq. (9.5) leads to the retrieval of refraction with an accuracy of about 0.02% [27]. Leick [26, p. 196] provides an explanation of Eq. (9.5) as follows: the first term is the sum of the *distortion* of the electron charges of the dry gas molecules under the influence of a magnetic field, the second term expresses the same effect, but for water vapour, while the third term describes the permanent dipole moment of the water vapour, i.e., it is a direct result of the geometry of water vapour's molecular structure. The *first term* of Eq. (9.5) is then divided into two parts to give [26, p. 196]:

1. the refractivity of an ideal gas in hydrostatic equilibrium, i.e., *hydrostatic refractivity*, which is the larger component and can be accurately computed if the surface total pressure is available, and
2. a function of *partial water vapour pressure*. This is the smaller component of the two and has to be either measured or estimated (e.g., Fig. 9.1).

The division is achieved using the equation of the state of a gas

$$p_i = Z_i \rho_i R_i T, \; for \; i = \{d, wv\}, \tag{9.6}$$

with ρ_i being the mass density and R_i the specific gas constant. In Eq. (9.6), the subscripts d, and wv represent dry gas and water vapour, respectively. Using this equation in (9.5), it is immediately noticeable that the term P_d in the first part can be replaced. This introduces the density term ρ_d, which can then be replaced by the total density ρ and partial density of water vapour ρ_{wv}. Replacing this partial density of water vapour ρ_{wv} by Eq. (9.6) leads to the division of the first term as [26, p. 196]

$$k_1 \frac{P_d}{T} Z_d^{-1} = k_1 R_d \rho - k_1 \frac{R_d}{R_{wv}} \frac{P_{wv}}{T} Z_{wv}^{-1}, \tag{9.7}$$

which clearly indicates that the refractivity of the hydrostatic term is due to both dry gas and partial water vapour, as had been previously stated, e.g., by [9]. When (9.7) is substituted into Eq. (9.5) and combined with the second term of (9.5), one obtains

$$N = k_1 R_d \rho + k_2^{'} \frac{P_{wv}}{T} Z_{wv}^{-1} + k_3 \frac{P_{wv}}{T^2} Z_{wv}^{-1}, \tag{9.8}$$

and

$$k_2^{'} = k_2 - k_1 \frac{R_d}{R_{wv}} = k_2 - k_1 \frac{M_{wv}}{M_d}, \tag{9.9}$$

with M_i, $i = \{d, wv\}$ being the molar mass. Equation (9.8) essentially provides the *hydrostatic* (N_d) and *wet refractivity* (N_{wv}) terms, respectively, as

$$N_d = k_1 \frac{P}{T}, \tag{9.10}$$

and

$$N_{wv} = k_2^{'} \frac{P_{wv}}{T} Z_{wv}^{-1} + k_3 \frac{P_{wv}}{T^2} Z_{wv}^{-1}. \tag{9.11}$$

Integrating (9.5) along the zenith direction using (9.10) and (9.11) gives the zenith hydrostatic delay (ZHD) and the zenith wet delay (ZWD), respectively, as [26, p. 197]

$$ZHD = 10^6 \int_{antenna}^{\infty} N_d(h) \mathrm{d}h, \tag{9.12}$$

$$\boxed{ZWD = 10^6 \int_{antenna}^{\infty} N_{wv}(h) \mathrm{d}h}. \tag{9.13}$$

For satellites that are not vertically overhead, i.e., not in the direction of the zenith, the hydrostatic and wet delays in (9.12) and (9.13) have to be converted into the equivalent slant delays through

$$\begin{aligned} SHD &= ZHD.mf_h(\alpha) \\ SWD &= ZWD.mf_{wv}(\alpha), \end{aligned} \tag{9.14}$$

leading to the slant total delay (STD) expressed as

$$STD = SHD + SWD, \tag{9.15}$$

where mf_h and mf_{wv} are mapping functions and α is the elevation angle. Note that the zenith angle $(90 - \alpha)$ could also be used. The simplest relation between the wet delay (SWD) along a line of elevation angle α and the ZWD is given through the simple pythagorean

$$\boxed{SWD = \frac{ZWD}{sin(\alpha)}}. \tag{9.16}$$

The most commonly used mapping function is Niell's [28]. Using the zenith angle z, Niell's mapping functions $mf_h(z)$ and $mf_{wv}(z)$ are given by [28]

$$mf_h = \frac{1 + f_1}{cos(z) + f_2} + h\left(\frac{1}{cos(z)} - \frac{1 + f_3}{cos(z) + f_4}\right), \tag{9.17}$$

and

$$mf_{wv}(z) = \frac{1 + f_5}{cos(z) + f_6}, \tag{9.18}$$

where

$$f_1 = \frac{a}{1 + \left(\frac{b}{1+c}\right)}$$

$$f_2 = \frac{a}{cos(z) + \left(\frac{b}{cos(z)+c}\right)}$$

$$f_3 = \frac{a_h}{1 + \left(\frac{b_h}{1+c_h}\right)}$$

$$f_4 = \frac{a_h}{cos(z) + \left(\frac{b_h}{cos(z)+c_h}\right)}$$

$$f_5 = \frac{\tilde{a}}{1 + \left(\frac{\tilde{b}}{1+\tilde{c}}\right)}$$

$$f_6 = \frac{\tilde{a}}{cos(z) + \left(\frac{\tilde{b}}{cos(z)+\tilde{c}}\right)},$$

where a, b, and c are the coefficients of the hydrostatic mapping function given in Niell [28, Table 3], while $\tilde{a}$, $\tilde{b}$, and $\tilde{c}$ are the coefficients of the wet mapping function in Niell [28, Table 4]. Tropospheric delay is thus shortest in the zenith direction where the elevation angle $\alpha = 90°$, but increases as the elevation angle decreases.

From the STD, which can be estimated from GPS observations, the measurable signals of interest to environmental monitoring are the *precipitable water* (PW) and the *integrated water vapour* (IWV). Let us now consider that for each receiver of the continuous operating reference stations (CORS; see Sect. 5.5), Eq. 4.18 from p. 49 applies. For a known station, the range between the satellite and the receiver will be accurately known. If the other errors discussed in Sect. 3.4 are properly modelled, the remaining residual errors of the observations will be due to STD, see e.g., [26]. These STD could then be used to estimate ZWD given a proper mapping function and assuming that the ZHD has been accurately obtained from surface meteorological measurements. The estimation of ZWD from GNSS observation equations can take on the form of [29, 30]:

(i) *Least squares solution* (see Sect. 6.3) where the ZWDs are obtained as unknowns, i.e., the deterministic approach from which one parameter is estimated per station per specified time interval. This approach involves constraining the value of the ZWD and perhaps its rate of change, to keep it within a reasonable set of bounds [29].

(ii) Estimation as a *stochastic process* using a Kalman filter [31], where the temporal variation of ZWD is assumed not to change by a large amount over a short period of time. The stochastic filter estimation of ZWD requires a proper choice of the

stochastic process that represents its fluctuation. One common choice is the first-order Gauss–Markov process and the stochastic noise is chosen so as to constrain the variation of the ZWD to between 1 and 20 mm per hour, depending on location and the time of the year [29].

As we shall see in Sect. 11.3.2, NWP models require precipitable water and as such the conversion of the GNSS measured ZWD to precipitable water vapour (PWV) and integrated water vapour (IWV) is necessary. Askne and Nordius [32] have shown that it is possible to relate IWV and the measured ZWD. The relationship is presented by Belvis et al. [29] as

$$IWV \approx \zeta ZWD \tag{9.19}$$

and

$$\boxed{PWV = \frac{\zeta ZWD}{\rho}}, \tag{9.20}$$

where ρ is the total density. In (9.19) and (9.20), the value of the constant ζ, i.e., the ratio IWV/ZWD, varies between 5.9 and 6.6 and is given by [26, p. 201] as

$$\frac{1}{\zeta} = 10^{-6}\left(\frac{k_3}{T_m} + k_2'\right) R_{wv}, \tag{9.21}$$

where T_m is the weighted mean temperature of the atmosphere given by

$$T_m = \frac{\int \frac{P_{wv}}{T} Z_{wv}^{-1} dh}{\int \frac{P_{wv}}{T^2} Z_{wv}^{-1} dh}. \tag{9.22}$$

In estimating PWV from (9.20), the largest source of error is attributed to the mean temperature T_m, which varies with *location*, *height*, *season*, and *weather*. Belvis et al. [29] provided a total error budget of the estimated ZWD of ~ 10 mm random error and ~ 10 mm long-term bias. This was based on the comparison of the results of Very Long Baseline Interferometry (VLBI), GPS, and WVR (water vapour radiometers), with the error component divided as follows [29]:

(a) 5% error due to the inversion from path delay to IWV in non-arid areas.
(b) Errors of less than 10 mm in path delay arising from carrier-phase measurements and propagated through the Kalman filtering estimation method.
(c) Errors of the order of 3 mm in ZWD under normal ionospheric conditions arising from the use of dual-frequency signals for range correction (i.e., ionospheric correction).
(d) Less than 1% (23 mm) errors in hydrostatic delay as a result of atmospheric dynamics. Proper station calibration, however, can potentially reduce this error to less than 1 mm.

(e) Multipath errors will depend on the type of antenna, elevation angle of the satellites and the environment in which the antenna is located. Belvis et al. [29] suggest that since this error is normally less than 100 mm for elevation angles of 15°, it is likely to perturb the zenith delay measurement by less than 20 mm.
(f) The contribution of ionospheric effects on the signal will generally be below the total error budget.

9.2.3 GNSS Remote Sensing Techniques

Over the years, research efforts have been dedicated to modelling atmospheric refraction in order to improve on GNSS positioning accuracy by accounting for the excess path delay in Eq. (9.2). As we discussed in Sect. 3.4.3, modelling of the propagation delay is done separately for the *ionosphere* and *troposphere*. For the ionosphere, Eqs. (3.5) and (3.6) on p. 37 are applied to eliminate most of the ionospheric delay. For the tropospheric delay on the other hand, we saw that the troposphere is a non-dispersive medium and that its delay could not be eliminated by the linear combination of dual-frequency observations, but must instead be measured or estimated. In the next sections, we present both space and ground based GNSS remote sensing methods and related missions, which are essential in measuring the atmospheric parameters discussed in Sect. 9.2.2.

9.2.3.1 Space-Borne GNSS Remote Sensing

GNSS radio occultation (GNSS-RO) takes place when a transmitting satellite, setting or rising behind the Earth's limb, is viewed by a LEO satellite as illustrated in Fig. 9.2. GNSS satellites send radio signals that pass through successively deeper layer of the

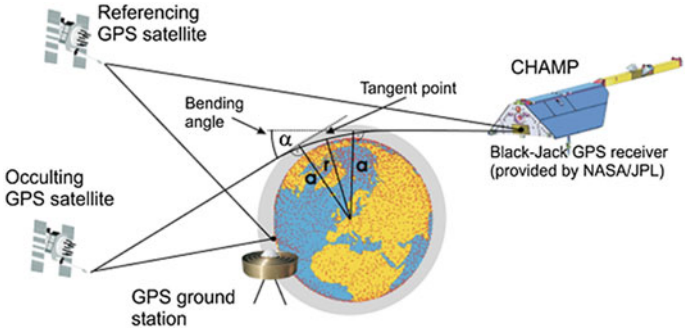

Fig. 9.2 GNSS radio occultation. Use is made of (i) an occulting satellite, (ii) a non-occulting GNSS satellite and (iii) a ground-based GNSS station to determine the bending angle α from which the vertical profiles of temperature and pressure are determined, e.g., from Eq. 9.4 on p. 144. *Source* Wickert [3]

Earth's atmosphere and are received by LEO satellites. These signals are bent and retarded, causing a delay in their arrival at the LEO.

Figure 9.2 shows the occultation geometry where the signal transmitted from a GNSS to a LEO satellite passes through dispersive layers of the ionosphere and atmosphere, and in so doing senses them. As the signal is bent, the total bending angle, α, an impact parameter, a, and a tangent radius, r_t, define the ray passing through the atmosphere. The *refraction angle* is accurately measured and related to the atmospheric parameters; temperature, pressure and water vapour via the refractive index in Eq. 9.4. Use is made of radio waves where a GNSS receiver onboard a LEO satellite measures, at the required sampling rate, the dual-band carrier-phases (L1 and L2), the C/A-code and P-code group delay (see Sect. 3.3.1) [11, 12]. The data is then processed to remove errors arising from short-term oscillator and instabilities in the satellites and receivers. This is achieved by using at least one ground station and one satellite that is not being occulted, leading to a doppler shift (see Fig. 9.2). Once the observations have been corrected for possible sources of errors, the resulting *Doppler shift* is used to determine the refraction angle α.

The variation of α with a during an occultation depends primarily on the vertical profile of the atmospheric refractive index, which is determined globally by *Fermat's principle* of least time and locally by *Snell's law*

$$n \times sin\phi = constant, \tag{9.23}$$

where ϕ denotes the angle between the gradient of refraction and the ray path. The doppler shift is determined by projecting spacecraft velocities onto the ray paths at the transmitter and receiver so that atmospheric bending contributes to its measured value. Data from several GNSS transmitters and post-processing ground stations are used to establish the precise positions and velocities of the GNSS transmitters and LEO satellites. These derived positions and velocities are used to calculate the Doppler shift expected in the absence of atmospheric bending (i.e., were the signal to travel in a straight line). By subtracting the *expected* shift from the measured shift, one obtains the excess Doppler shift. Assuming local symmetry and with Snell's law, the excess Doppler shift, together with satellites' *positions* and *velocities*, are used to compute the values of the bending angles α with respect to the impact parameters a. Once computed, these bending (refraction) angles are related to the refractive index by

$$\alpha(a) = 2a \int_{r=r_0}^{r=\infty} \frac{1}{\sqrt{n^2 r^2 - a^2}} \frac{\mathrm{d}In(n)}{\mathrm{d}r} \mathrm{d}r, \tag{9.24}$$

which is then inverted using Abel's transformation to give the desired refractive index

$$n(r_0) = \exp\left[\frac{1}{\pi} \int_{a=a_0}^{a=\infty} \frac{\alpha(a)}{\sqrt{a^2 - a_0^2}} da\right]. \tag{9.25}$$

If the atmospheric temperature T and pressure P are provided from external source, e.g., from models and synoptic meteorological data, then the vertical water vapour density could be recovered from GNSS remote sensing data using Eq. (9.4) [11].

To demonstrate the capability of the method, the following examples show that the temperature profiles measured by GNSS around the tropopause region (8–17 km) gives accurate results comparable to the traditional radiosonde method.

Example 9.1 (Validating GNSS derived atmospheric parameters [33]).

In Fig. 9.3, GNSS-derived temperature profiles from LEO missions (COSMIC, CHAMP and GRACE) are compared with the profiles of the closest radiosondes in Australia. The radiosonde launched from Learmonth Airport (22.24°S, 114.09°E) on 14th June 2005 was within 70 km and 40 min from the CHAMP measurement, whereas the radiosonde launched from Hobart Airport (42.84°S, 147.50°E) on 20th December 2006 was within 12 km and 1.25 h from the COSMIC measurement. The radiosonde from Weipa Aero location and the GRACE RO profile were located within 92 km, with time difference of 1.25 h from each other.

A visual examination of Fig. 9.3 indicates that the COSMIC RO temperature profile agrees very well with its corresponding radiosonde profile with almost no deviation from the radiosonde data. The temperature profiles from the CHAMP satellite have been shown, e.g., by Schmidt et al. [34] to agree well in the upper troposphere and lower stratosphere. However, looking at Fig. 9.3, below 5 km, the CHAMP profiles do not fit the radiosonde data as well as those for the COSMIC profiles due to the effect of water vapour. The GRACE temperature profile agrees well with the corresponding radiosonde measurement above 8 km, while below 8 km it is also affected by water vapour like the CHAMP profiles.

♣ End of Example 9.1.

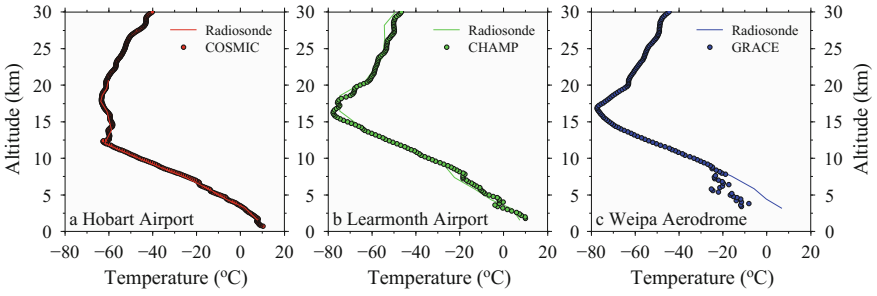

Fig. 9.3 GNSS-RO soundings observed on **a** 20 December 2006 over Hobart Airport [42.84°S, 147.50°E] using COSMIC RO data, **b** 14 June 2005 over Learmonth Airport in Western Australia [22.24°S, 114.09°E] using CHAMP RO data and **c** on 8 September 2006 over Weipa Aero using GRACE data [12.68°S, 141.92°E]. *Source* [33]

Example 9.2 (Comparison of profiles between 7–30 km height [33]).

GNSS-derived temperature profiles between 7–30 km were then compared to those from the radiosonde observations between 2001 and 2006. The comparison method was based on a maximum spatial separation of 100 km and a temporal difference of 3 h between the GNSS-RO measurements and the radiosonde (e.g., Schmidt et al. [34] use values between 3 h and a distance of 300 km, which they state would mean near constant weather). A distance of 100 km was chosen to account for the spatial drift of the radiosondes, which can reach as far as 200 km from its initial position [35]. Temperatures are compared at 14 standard pressure levels l of the radiosonde data files between 850 and 20 hPa.

The mean temperature deviation at each pressure level $\overline{\Delta T(l)}$ and its standard deviation $\sigma_{\Delta T}(l)$ are calculated according to Eqs. (9.26) and (9.27) [36].

$$\overline{\Delta T(l)} = \frac{\sum_{i=1}^{M(l)} T_{D(LEO)}(i,l) - T_{Radiosonde}(i,l)}{M(l) - 1} \tag{9.26}$$

$$\sigma_{\Delta T}(l) = \sqrt{\frac{1}{M(l) - 1} \sum_{i=1}^{M(l)} \left(T_{D(LEO)}(i,l) - T_{Radiosonde}(i,l)\right)^2}, \tag{9.27}$$

where $M(l)$ denotes the number of data points at each pressure level. The index i indicates the individual pairs of LEO satellite and radiosonde data, $T_{D(LEO)}$ is the dry temperature derived from the LEO data while $T_{Radiosonde}$ is the temperature given by radiosonde measurements. Temperature deviations exhibiting more than 20 K were ignored to eliminate the influence of outliers.

Figure 9.4 compares the deviation between the radiosonde and CHAMP, GRACE and COSMIC profiles, as well as the number of profiles. 80 CHAMP profiles from September 2001 to December 2006 were found to occur within 100 km and a time delay of less than 3 h of a radiosonde profile. The results of the comparisons indicate a temperature bias of less than 1 k for the complete height interval between 9 and 26 km, with a standard deviation of less than 2 K. Between 11 and 26 km the bias is less than 0.5 K with a standard deviation of 1–2 K. The bias of the CHAMP temperature in the lower troposphere (altitude < 7.5 km) is largely due to the presence of water vapour, see also [4, 36, 37]. The larger bias between CHAMP and radiosonde data is less than 0.5 k in the upper troposphere and lower stratosphere where there is little or no water vapour. Biases between CHAMP RO data and radiosonde data are all negative for all the altitude levels between 1.5 and 26 km.

Only 18 profiles from GRACE RO data from January 2006 to October 2007 were found within the defined spatial and temporal limits. Nevertheless, the bias is less than 3 K between the altitude range of 9 and 20 km, showing that GRACE RO data agrees well over this range with the radiosonde measurements. Below 9 km, like the CHAMP data, the GRACE temperature profiles are also affected by the presence of

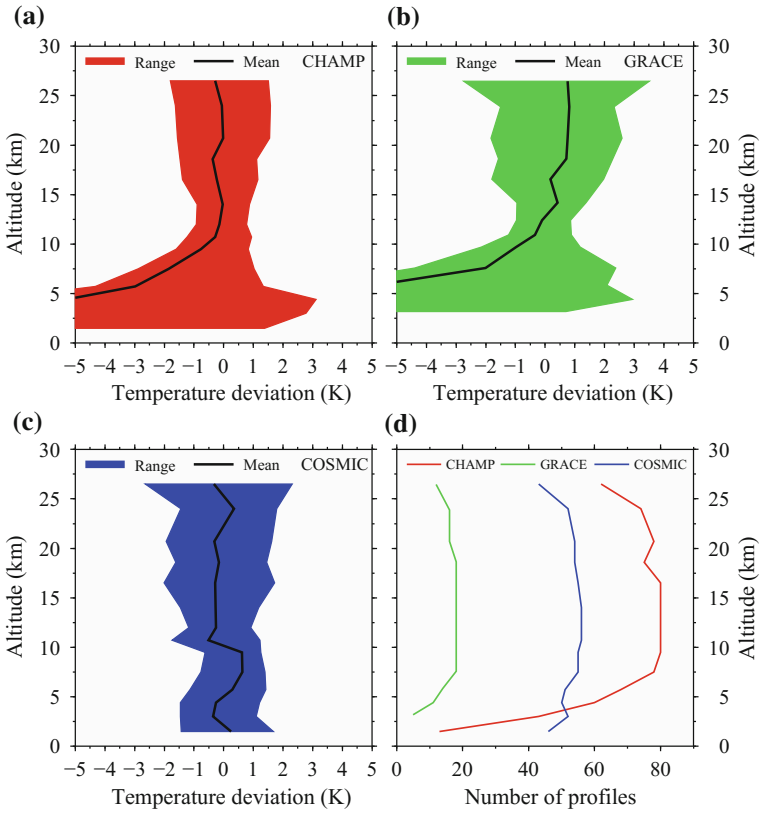

Fig. 9.4 Comparison of the deviations between GNSS-RO profiles **a** CHAMP, **b** GRACE, and **c** COSMIC profiles. **d** Number of profiles from each satellite. *Source* [33]

water vapour. However, the bias in the GRACE temperatures could be due to the lower number of GRACE profiles meeting the selection criteria.

COSMIC RO data from April 2006 to December 2006 were also used for these comparisons, with 54 COSMIC RO profiles meeting the criteria. From Fig. 9.4, it can be seen that the bias between CHAMP and COSMIC RO data agree well between 10.7 and 25 km, with the difference in the bias over this altitude range being less than 0.5 K. CHAMP RO data displays a lower standard deviation than COSMIC data between 10 and 18 km, with a standard deviation of less than 1.5 K. Below 7.5 km, CHAMP temperatures show a large negative bias whereas the bias from the COSMIC temperature remains constant.

From these three GNSS-RO data sets, the COSMIC temperature data provided a good correlation of data with much smaller standard deviations, with CHAMP and GRACE having higher standard deviations below 10 km. This example highlights the possibility of GNSS satellites being used to remote sense the atmosphere at the heights between 7–25 km with accuracies that will suffice for the environmental

monitoring of the atmosphere, specifically the tropopause, an issue that will be discussed in detail in the next chapters.

♣ End of Example 9.2.

Next, we look at the LEO satellite missions that make the GNSS space borne remote sensing possible. Several missions are currently operational, but we will present only the three most commonly discussed.

9.2.3.2 GNSS Radio Occultation Missions

The three LEO missions covered in this work; CHAMP, GRACE, and COSMIC, jointly contributed a total of 2 478 829 profiles between 2001 and 2008 that were analysed [38]. The German CHAMP (Fig. 9.9, left) satellite was launched on July 15, 2000 into an almost circular and near polar orbit (with an inclination of 87°) at an altitude of about 454 km [39]. The GNSS radio occultation on board CHAMP was activated on Febraury 11, 2001, and from then nearly 541,527 occultations were recorded worldwide by 2008 [38]. Having been in operation for more than a decade, CHAMP ended its mission on 19th of September 2010. CHAMP data can however still be obtained from GFZ (German Research Centre for Geosciences), the Jet Propulsion Laboratory (JPL) or the University Corporation for Atmospheric Research (UCAR).[3]

CHAMP Level 3 data (version 005) from GFZ data contains Abel inverted profiles of refractivity derived from the vertical profiles of bending angles. They also contain the environmental monitoring indicators of air temperature, air density, air pressure, bending angles, positions (latitudes, longitudes), heights above mean sea level, impact parameters, and signal to noise ratios (SNR) up to 30 km above mean sea level with a vertical resolution of 200 m.

Radio occultation measurements by GRACE satellites (Fig. 9.9, right), discussed in detail in Sect. 9.3.3, were first recorded during a 25 h period on July 28/29, 2004 [36, 40]. Atmospheric profiles derived from GRACE show nearly identical characteristics as those from the ECMWF (European Center for Medium-Range Weather Forecasts) [41]. The GRACE satellites had recorded over 141,987 occultations worldwide as of 2008 [38]. The BlackJack GNSS receiver present in the GRACE satellites enables deep atmospheric sounding into the lower troposphere. The GRACE level 2 data, obtainable from GFZ, is equivalent to that from CHAMP, with the same vertical resolution of 200 m.

GNSS limb sounding reached new heights after the launch of the COSMIC mission (see, Fig. 9.5) into a near circular orbit on April 15, 2006, e.g., [8, 42]. COSMIC, a constellation of six identical micro-satellites, is a joint mission between the National Space Organisation (NSPO) of Taiwan and UCAR in the United States, with the main goal of obtaining vertical profiles in near-real time of temperature,

[3] via http://www.cosmic.ucar.edu.

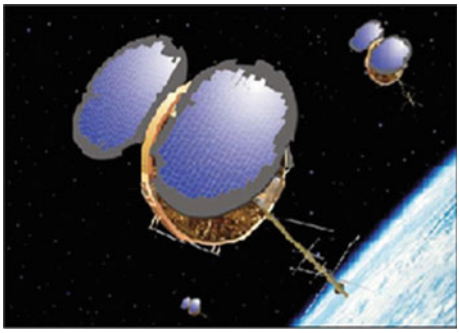

Fig. 9.5 The COSMIC-1 satellites. Cosmic-2 satellites are planned for launch in 2017 (6 satellites) and in 2020 (6 more satellites). *Source* http://www.cosmic.ucar.edu

pressure, and water vapour in the neutral atmosphere and electron density in the ionosphere [42]. One major change in the COSMIC data compared to CHAMP and GRACE is the improved data quality, with higher yields in the lower troposphere (below 7 km; cf. Figs. 9.3 and 9.4). This is made possible by the use of the Open-Loop (OL) signal tracking technique by the Black Jack GNSS receiver [41]. OL signal tracking, which was not available in previous missions, allows for the tracking of rising occultation and deeper penetration into the lower troposphere.

The COSMIC mission provides about 2200 profiles per day on average and by 2008, it had recorded about 1,796,315 [38, 41] and by 20th January 2017, it had recorded 4,436,178.[4] Level 2 COSMIC data can be obtained from both UCAR[5] and NSPO.[6] It contains the environmental monitoring indicators of refractivity, air temperature, water vapour, air pressure, height above mean sea level, and the position (latitude and longitude) from mean sea level to 400 km. The tropopause region from COSMIC (like CHAMP Level 3 data) contains temperatures, in which the water vapour is neglected. Level 2 COSMIC atmospheric profiles are provided with a vertical resolution of 100 m. In the following example, the number and distribution of GNSS-RO measured over Australia by 2008 from these missions are presented. Due to the success of COSMIC satellite mission that has operated for more than a decade, U.S. agencies and Taiwan have decided to move forward with a follow-on RO mission (called FORMOSAT-7/COSMIC-2) that will launch six satellites into low-inclination orbits in 2017, and another six satellites into high-inclination orbits in 2020.[7]

Example 9.3 (Distribution of GNSS-RO over Australia by 2008 [33]).

The distribution of the GNSS-RO events depends on the geometry of the orbits of the LEO satellites and the transmitting GNSS satellites. CHAMP RO events occured

[4] http://www.cosmic.ucar.edu/index.html.

[5] via http://www.cosmic.ucar.edu.

[6] via http://www.tacc.cwb.gov.tw.

[7] http://www.cosmic.ucar.edu/cosmic2/index.html.

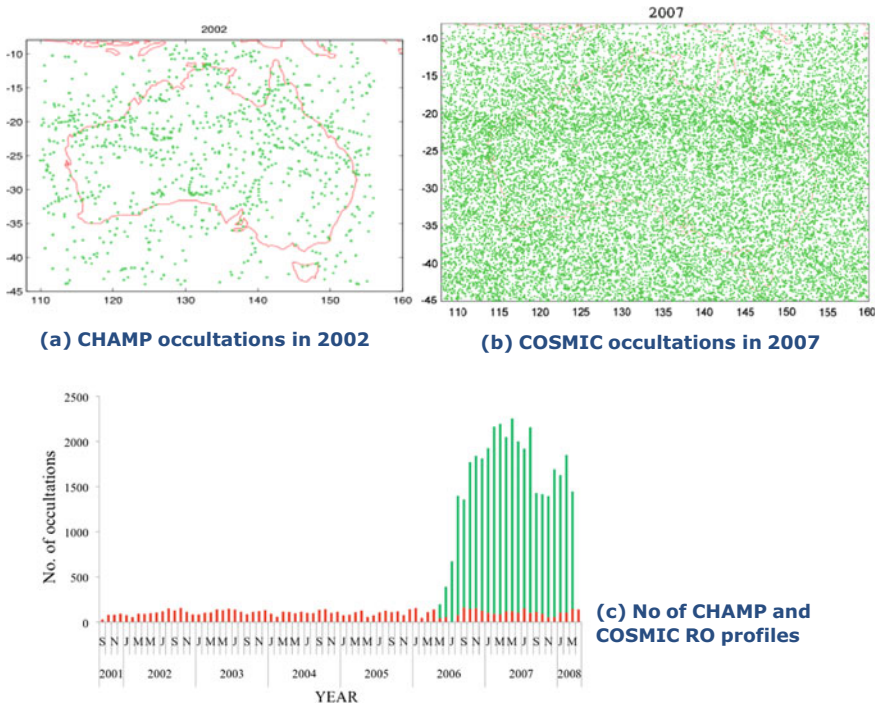

Fig. 9.6 Number of radio occultations over Australia from **a** CHAMP in 2002, **b** COSMIC in 2007, and **c** total number of occultations for CHAMP and COSMIC from 2001 to 2008. It can be seen that COSMIC provided a very dense coverage within its two years of existence. *Source* [33]

more commonly in high latitudes, with the exception of the poles, with a relatively low distribution in the equatorial regions, e.g., [4, 43]. From the start of September 2001 to April 2008 for example, Australia was covered by 8,472 CHAMP RO profiles, averaging about 108 occultations per month, except for July 2006 (Fig. 9.6). Figure 9.6 indicates that the occultations are well distributed over Australia, although with fewer data in the far north, a fact already pointed out by [43]. It can be seen from Fig. 9.6 that the COSMIC occultations are also well distributed across the region. Like CHAMP RO data, the COSMIC RO profiles are also fewer nearer to the equator (8–15°S).

♣ End of Example 9.3.

9.2.3.3 Ground-Based GNSS Remote Sensing

Whereas GNSS receivers are onboard LEO satellites (e.g., CHAMP and GRACE) in space-borne GNSS remote sensing, they are fixed to ground stations in the case

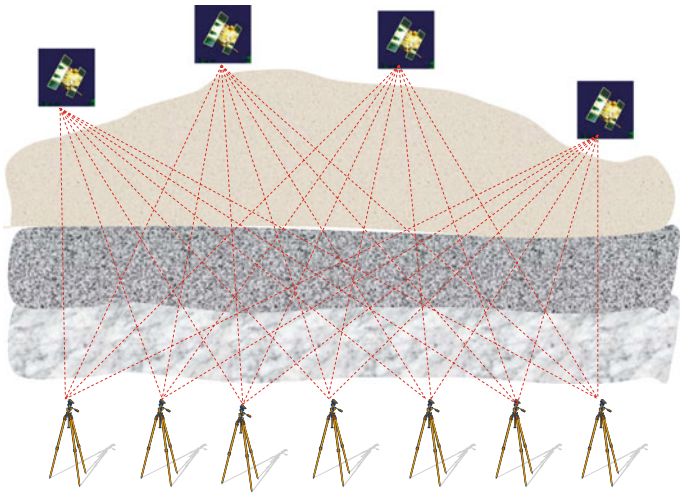

Fig. 9.7 Schematic diagram showing the remote sensing of water vapour via ground-based GNSS receivers. Figure 5.12 on p. 81 presents an example of a GEONET ground-based station

of ground-based GNSS remote sensing (Fig. 9.7). As we indicated in Sect. 3.4.3, the contribution of the *hydrostatic part*, which can be modeled and eliminated very accurately using surface pressure data or three-dimensional numerical models, is about 90% of the total delay, while that of the wet delay is highly variable with little correlation to surface meteorological measurements, see also [27, 44].

Assuming that the *wet delay* can be accurately derived from GNSS data as discussed in Sect. 9.2.2, and that reliable surface temperature data are available, the wet delay can be converted into an estimate of the total atmospheric water vapour P_w present along the GNSS ray path, as suggested by Belvis et al. [29]. This atmospheric water vapour P_w, termed *precipitable water* in GNSS-meteorology, is obtained using Eq. (9.20) on p. 149.

Using several receivers to track several satellites (see Fig. 9.7), a three-dimensional distribution of water vapour and its temporal variation can be quantified. For example, the Japanese GEONET CORS network (Fig. 5.14 on p. 85) is dedicated to ground-based GNSS meteorology, e.g., [17, 45]. The dense network of GNSS receivers is capable of delivering information about atmospheric water vapour content, which is useful to meteorological monitoring (e.g., climate studies and weather forecasting discussed in Sect. 11.4). Hanssen et al. [46] point out that maps of the water vapor distribution associated with, for example, a precipitating cloud, a partly precipitating cold front, or horizontal convective rolls, reveal quantitative measurements that are not observable with conventional methods.

Example 9.4 (Global validation of GNSS-derived water vapor [47]).

Heise et al. [47] provides an overview of the *data processing* and *retrieval* of vertical refractivity, temperature and water vapor profiles from GNSS radio occultation observations. They also undertook a global validation of CHAMP water vapor profiles with radiosonde data and obtain a bias of about 0.2 g/kg and a standard deviation of less than 1 g/kg specific humidity in the lower troposphere, thus demonstrating the potentials of GNSS-derived CHAMP retrievals for monitoring the mean tropospheric water vapor distribution on a global scale.

♣ End of Example 9.4.

9.3 GNSS Contribution to Remote Sensing of Gravity Variations

In the subsections that follow, it is explained how GNSS satellites (particularly GPS) support LEO satellites used to monitor variations in gravity field, which are in turn used to remote sense the changes in stored water at continental scales. The most significant success of a LEO satellite is evidenced in the GRACE satellites discussed in Sect. 9.3.3. A possible use of GNSS satellites to measure variations in water mass is illustrated by Tregoning et al. [48] whose predictions derived from GRACE measured fields show a correlation with GNSS measured deformations, suggesting the possible use of such deformations to infer changes in stored water potential on much shorter temporal and spatial scales than GRACE provides (and with low-latency), while averaging over much larger spatial scales than afforded by multipath amplitude measurements [10].

9.3.1 Mass Variation and Gravity

Two types of gravity field variation exists. The *first* is the long-term, also known as mean gravity field, which is due to the static part of the gravity field. The variation is constant over a very long time interval. Its study is useful in understanding the solid structure of the Earth, ocean circulation, and in achieving a universal height measuring system. In this respect, GNSS satellites are used to position LEO satellites such as GOCE (Gravity field and the steady state-of-the ocean circulation explorer, Fig. 9.8), which maps changes in gravity using state-of-the-art gradiometer with improved accuracy, see e.g., Hirt [49]. GOCE data is expected to benefit other studies such as those concerned with earthquakes, changes in sea level, and volcanoes.[8]

[8] See, e.g., http://www.esa.int/esaCP/SEMV3FO4KKF_Germany_0.html.

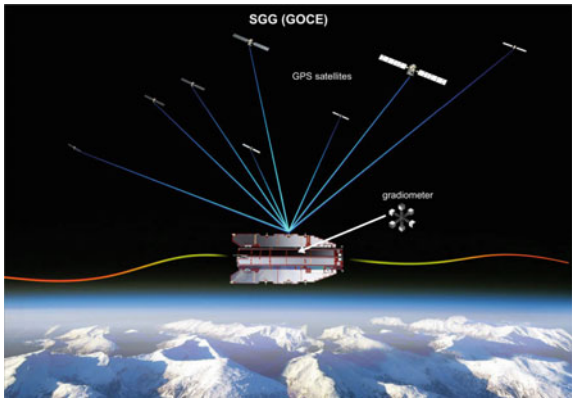

Fig. 9.8 GNSS satellites track the GOCE satellite in space, thus contributing to the determination of its position (©ESA). The GOCE satellite's accurate determination of the static gravity field is expected to contribute towards studies of changes in sea level, earthquakes, and volcanoes. Figure modified by D. Rieser [50]

The *second* type of variation of the Earth's gravity field is associated with those processes that occur over shorter time scales, such as atmospheric circulation or the hydrological cycle. This is known as the *time-varying gravity field* and is the component which enables the monitoring of, for example, variations in water resources and the melting of the polar ice.

By removing the effects of the other processes that cause changes in the gravity field, changes in *terrestrial water storage* can thus be inferred from the observed temporal changes in the terrestrial gravity field. By assuming the density of water as $1.00\,\mathrm{g/cm^3}$, and following the relation of [51], Ellet et al. [52] present the relationship between changes in stored water and gravity as

$$\Delta S = 0.419 \Delta g, \tag{9.28}$$

where water storage change ΔS is given in units of cm of water and gravity change Δg is in units of microGal (10^{-6} cm/s^2). From Eq. (9.28), it is seen therefore, that monitoring variations in the gravity field can enable hydrological changes to be monitored.

9.3.2 High and Low Earth Orbiting Satellites

At the broadest conceptual level, LEO satellites' gravity field missions observe (either directly or indirectly) gradients in the Earth's external gravitational field. This is essentially done through differential measurements between two or more points, thus largely eliminating spatially correlated errors (cf. differential GPS in Chap. 5). When done from space, two approaches can be used, e.g., [53, 54]:

1. Satellite-to-satellite tracking (SST), or
2. A dedicated gravity gradiometer on board a satellite, coupled with SST.

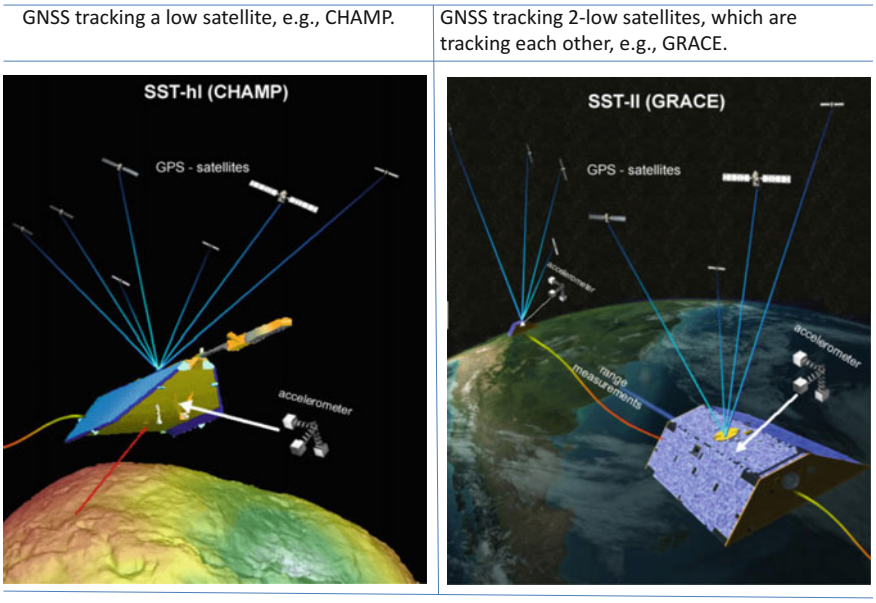

Fig. 9.9 *Left* SST-hl realized with CHAMP (©GFZ Potsdam ([2.2]). *Right* A combination of ll-SST and hl-SST realized with GRACE and GNSS satellites(©GRACE - CSR Texas ([2.2]). Figures modified by D. Rieser [50]). GNSS satellites are used in determining the positions of these satellites in space. For the GRACE satellites (*right*) inter-satellite distances can be computed from these positions and compared to the measured K-band distances, thus providing additional independent information

The SST methods can use either low-low inter-satellite tracking (ll-SST, see Fig. 9.9, right), where two LEO satellites track one another and additional observations in terms of high precision ranges and range rates between the two satellites are taken, or high-low inter-satellite tracking (hl-SST, see Fig. 9.9), where high-Earth orbiting satellites (notably GPS) track a LEO satellite. The low-low mode, compared to the high-low mode, has the advantage of signal amplification leading to a higher resolution of the obtained gravity variations, up to the medium wavelength spectrum of a few hundred km in spatial extent [53]. Taking this further, a combination of ll-SST and hl-SST is conceptually better still, as is currently demonstrated by the GRACE mission (Fig. 9.9, right) with a baseline length between the two satellites of about 220 km. This is treated in detail in the next section.

In order to detect temporal gravity field variations at smaller spatial scales, the satellite(s) being tracked must be in as-low-as-possible orbits (close to the mass source), with the satellites being as free as possible from the perturbing effects of atmospheric drag [53]. In addition, so-called de-aliasing models (for correcting short-term - 6 h - variations due to atmosphere and ocean mass variations) have to be used to mitigate the propagation of unwanted signals (e.g., leakage from the oceans) into the derived gravity solutions, e.g., [55].

9.3.3 Gravity Recovery and Climate Experiment

The GRACE mission, launched on 17th of March 2002, consists of two near-identical satellites following one another in nearly the same orbital plane (about 400 km altitude) separated by a distance of 220 km; the so-called tandem formation (see Fig. 9.9, right). The ll-SST is measured using K-band ranging, coupled with hl-SST tracking of both satellites by GNSS (GPS; Fig. 9.9, right). GNSS receivers are placed on GRACE satellites to measure occulted signals (see Sect. 9.2.3.1), and also to determine the orbital parameters of GRACE satellites required in order to determine gravity changes. On-board accelerometers monitor orbital perturbations of non-gravitational origin (see, e.g., Sect. 4.1).

GRACE mission processes GNSS data to contribute to the recovery of long-wavelength gravity field, remove errors due to long-term onboard oscillator drift, and aligns measurements between the two spacecraft [56, p. 200]. The timing function of GNSS for precision orbit determination, in terms of position and velocity as a function of time, enable orbits to be determined within an accuracy better than 2 cm in each coordinate [56, p. 200]. These precise locations of the two satellites in orbit allows for the creation of gravity maps approximately once a month.[9] These gravity maps, when converted to total water storage maps, are useful for monitoring changes in stored water potential as demonstrated in Chap. 14.

The Earth's gravity field is mapped by making accurate measurements of changes in the distance between the satellites, using GNSS and a microwave ranging system. These changes in the distances between the two satellites occur due to the effect of the gravity (mass concentration) of the Earth. As the lead satellite passes through a region of mass concentration, it is pulled away from the trailing satellite (Fig. 9.9, right). As the trailing satellite passes over the same point, it is pulled towards the lead satellite thus changing the distance between the satellites.

Time-variable gravity field solutions are obtained by the exploitation of GRACE observation data over certain time intervals, i.e., every month [57, 58], or less, e.g., [59, 60]. There are a number of institutions delivering GRACE products, each applying their own processing methodologies and, often, different background models. The mission is currently providing scientists with an efficient and cost-effective way to monitor time-varying component of the gravity field with unprecedented accuracy and in the process yield crucial information about the distribution and flow of mass within the Earth system. The process causing gravity variations that are currently being studied by GRACE include [61];

- changes due to surface and deep currents in the ocean leading to more information about ocean circulation, e.g., [62, 63],
- changes in groundwater storage on land masses, relevant to water resource managers, e.g., [61, 64–66, see also Chap. 14],

[9] http://www.csr.utexas.edu/grace/publications/brochure/page11.html.

- exchanges between ice sheets or glaciers and the oceans, needed for constraining the mass balance of the global ice regime and sea level change, e.g., [67, 68, see also Sect. 11.4.4],
- air and water vapour mass change within the atmosphere, vital for atmospheric studies, e.g., [69, 70], and
- variations of mass distribution within the Earth arising from, e.g., on-going glacial-isostatic adjustments and earthquakes, e.g., [71, 72].

Currently, river basins of the order of 200,000 km^2 and above in area can be successfully studied using the GRACE products [73]. In general, to understand how the GRACE satellites monitor changes in fresh water (all groundwater, soil moisture, snow, ice, and surface waters), first, the larger effect of the mass of the Earth, i.e., the static gravity field discussed in Sect. 9.3.1, which is always a constant G_0 corresponding to nearly 99% of the total field, is computed from a static model (e.g., *GGSM01S* [58]) and removed by subtracting it from the monthly gravity field ($G(t)$) measured by GRACE at a time t [74], i.e.,

$$\Delta G(t) = G(t) - G_0, \tag{9.29}$$

to give the monthly time-variable gravity field $\Delta G(t)$. Changes mostly related to the atmosphere and ocean, which occur over timescales shorter than one month, are then removed using models, see e.g., Wahr et al. [75]. Remnant atmospheric and oceanographic effects that last for more than one month can be removed using atmospheric and ocean circulation models before water storage change can be analyzed. The resulting difference in Eq. (9.29), which is called the gravity field anomaly is usually due to changes in stored water. If we consider $\overline{\Delta C}_{nm}(t)$ and $\overline{\Delta S}_{nm}(t)$ to be the normalized Stokes coefficients expressed in terms of millimeters of geoid height, with n and m being degree and order respectively, the time-variable geoid in (9.29) is then expanded in-terms of spherical harmonic coefficients (see [76]) as

$$\Delta G(t) = \sum_{n=1}^{N} \sum_{m=0}^{n} (\overline{\Delta C}_{nm}(t) cos(m\lambda) + \overline{\Delta S}_{nm}(t) sin(m\lambda)) \overline{P}_{nm}\,(cos(\theta))\,, \tag{9.30}$$

where N is the maximum degree of expansion, θ is the co-latitude, λ the longitude and $\overline{P}_{nm}$ the fully normalized Legendre polynomial [76]. From the gravitational spherical harmonic coefficients (9.30), the equivalent water thickness is computed using the following steps:

1. The gravitational residual coefficients are converted into the surface density coefficient differences by [75]

$$\begin{pmatrix} \Delta \check{C}_{lm}(\mathrm{M}_j) \\ \Delta \check{S}_{lm}(\mathrm{M}_j) \end{pmatrix} = \frac{\rho_{\mathrm{avg}}}{3\rho_{\mathrm{w}}} \frac{2l+1}{1+k'_l} \begin{pmatrix} \Delta \bar{C}_{lm}(\mathrm{M}_j) \\ \Delta \bar{S}_{lm}(\mathrm{M}_j) \end{pmatrix}, \tag{9.31}$$

where k'_l is the *load Love* number of degree l, $\rho_{\text{avg}} = 5517\,\text{kg/m}^3$ the average density of the Earth, and $\rho_{\text{w}} = 1000\,\text{kg/m}^3$ the density of water.

2. The spatial variation of the surface density is then computed through

$$\Delta\sigma(\theta, \lambda, \text{M}_j) = R\rho_{\text{w}} \sum_{l=1}^{l_{\max}} \sum_{m=0}^{l} [\Delta\check{C}_{lm}(\text{M}_j) \cos m\lambda + \Delta\check{S}_{lm}(\text{M}_j) \sin m\lambda] \bar{P}_{lm}(\cos\theta), \tag{9.32}$$

where $R = 6378137\,\text{m}$ is the radius of the Earth and $\Delta\sigma$ is in kg/m^2.

3. Finally, the changes in total water storage (TWS) are calculated by

$$\text{TWS}(\phi, \lambda, \text{M}_j) = \frac{\Delta\sigma(\theta, \lambda, \text{M}_j)}{\rho_{\text{w}}} = \frac{\Delta\sigma(\theta, \lambda, \text{M}_j)}{1000} \quad \text{[meters]}. \tag{9.33}$$

The first steps in the analysis of GRACE data would provide an estimate of the changes in total water storage. In the second step, the changes can then be separated into their various components as discussed, e.g., in [61, 74] to obtain changes in the respective components (e.g., groundwater, surface water, soil moisture, and ice).

The GRACE satellites have now well exceeded their planned 5 year life-span, however, plans are underway to launch a GRACE follow-on mission (GRACE-FO) around 2017 given the excellent results that have been delivered so far, see e.g., [38]. Although GRACE-FO satellites, like their predecessor, will use the same kind of microwave ranging system giving a similar level of precision, they will also test an experimental instrument using lasers instead of microwaves, which promises to make the measurement of their separation distance at least 20 times more precise[10]. In Yang [77], GRACE products are used to constrain recent freshwater flux from Greenland where the data show that Arctic freshwater flux started to increase rapidly in the mid-late 1990s, coincident with a decrease in the formation of dense Labrador Sea Water, a key component of the deep southward return flow of the Atlantic Meridional Overturning Circulation (AMOC). Recent freshening of the polar oceans may be reducing formation of Labrador Sea Water and hence may be weakening the AMOC [77].

9.4 Satellite Altimetry

9.4.1 Remote Sensing with Satellite Altimetry

Satellites altimetry (Fig. 9.10) operates in two steps:

- *First*, the precise orbit of the satellite, i.e., its position, is determined. Through this, its *height* above the Earth is obtained.

[10] http://gracefo.jpl.nasa.gov/mission/.

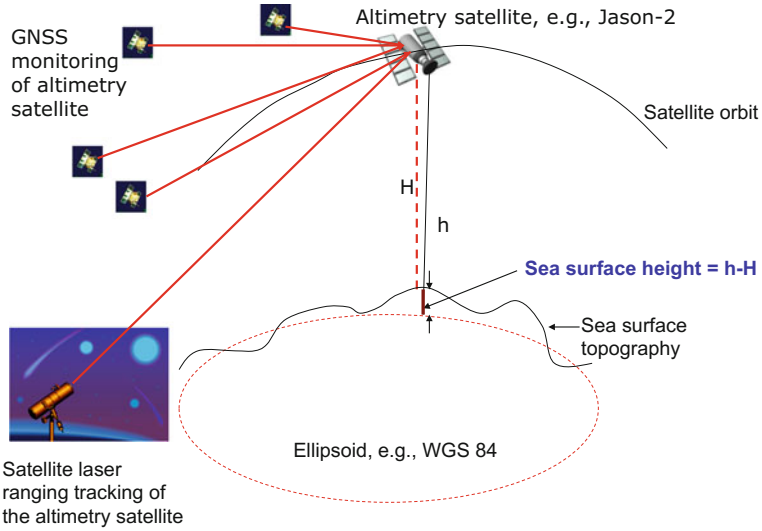

Fig. 9.10 GNSS in support of monitoring changes in sea level through the determination of the altimetry satellites' precise orbit. From the precise orbital parameters, the height component h is useful in determining changes in sea level through the difference $\{h - H\}$, where H is measured by multiplying the speed of light with the time taken by the signals to travel from and to the satellite divided by 2, since the same distance is covered twice

- *Second*, range measurements are made by obtaining the time an emitted signal (radar or laser) travels to the Earth's surface and reflected back to the satellite.

GNSS contributes to the *first step* where height is determined. This is achieved through GNSS receiver onboard the space satellites that enables monitoring of ranges and timing signals from GNSS satellites (see Sect. 4.2). The observed GNSS ranges provide precise and continuous tracking of the spacecraft, thereby delivering its position $\{\phi, \lambda, h\}$ at any time. The height component h is useful in determining the measured height (see Fig. 9.10). Besides GNSS tracking, other approaches such as satellite laser ranging (SLR) and DORIS (Doppler Orbitography and Radio positioning Integrated by Satellite) are also used to ensure that precise orbit determination is achieved.

In the *second step*, the Earth's surface heights (e.g., ocean surface, glaciers, and ice sheets) are measured using ranges from the space altimetry satellite to the surface of interest. Radar altimeters send microwave signals to the Earth's surface and measures the time taken by the reflected signals to travel back. Using Eq. (3.1), the distance from the satellite to the Earth's surface is derived. Since the signals pass through the atmosphere from and to the satellites, they are affected by the atmosphere (see Sect. 3.4.3) and as such, atmospheric corrections again have to be made. The sea surface height is then obtained by subtracting the measured ranges in step 2 from the GNSS-derived satellite heights in step 1 (Fig. 9.10).

9.4.2 Satellite Altimetry Missions

Direct use of GNSS to measure the annual changes in mass loss of the Greenland ice sheet is demonstrated in the work of Yang [77] who uses coastal uplift observed by GPS whose results show both spatial and temporal variations of coastal ice mass loss and suggest that a combination of warm atmospheric and oceanic condition drove the variations. Changes in ice sheet have been monitored using satellite altimetry among other methods. The first true altimetry mission was TOPEX/Poseidon, developed by NASA and the Centre National d'Etudes Spatiales (CNES) and launched on 10 August 1992. Its mission ended in 2006 after 13 years of operation, providing 11 years of data. It was followed by Jason-series (Jason-1 was launched on 07/12/2001 and Jason-2 on 20/06/2008). Both TOPEX/Poseidon and Jason-1 were dedicated to measuring global mean sea level from space. TOPEX/Poseidon orbited at 1336 km above the Earth and covered the global oceans every 10 days, measuring the heights of the ocean surface directly underneath the satellite with an accuracy of 2–4 cm or better when averaging over several measurements [78]. Jason-2 is expected to be replaced by Jason-3 launched on 17th of January 2016, and subsequently Sentinel-6. Sentinel-6 will continue high precision ocean altimetry measurements in the 2020–2030 time-frame using two successive, identical satellites (Jason-Continuity of Service): Jason-CS-A and Jason-CS-B, and as a secondary objective, collect high resolution vertical profiles of temperature using the GNSS Radio-Occultation sounding technique discussed in Sect. 9.2.3.1.[11] Combined, all these satellites will provide long-term series of data capable of undertaking *climatological studies* resulting from changes in sea level.

ICESat (launched on January 12, 2003) uses a 1064 nm-laser operating at 40 Hz to make measurements at 172-m intervals over ice, ocean, and land [79]. It combines state-of-the-art laser ranging capabilities with precise orbit and attitude control and knowledge to provide very accurate measurements of ice sheet topography and elevation changes along track. It has the specific objective of measuring changes in polar ice as part of NASA's Earth Observing System.

By observing changes in ice sheet elevation, it is possible to quantify the growth and shrinkage of parts of the ice sheets with great spatial detail, thus enabling an assessment of ice sheet mass balance and contributions to sea level. Moreover, because the mechanisms that control ice sheet mass loss and gain in accumulation, surface ablation, and discharge presumably have distinct topographic expressions, ice sheet elevation changes also provide important insights into the processes causing the observed changes [79]. ICESat-2 schedule for launch in 2017 is expected to be a follow-on mission to ICESat (Fig. 9.11) with improved laser capability compared to ICESat and will have the objectives of measuring ice sheet changes, sea ice thickness, and vegetation biomass. Achieving these objectives will contribute to the following [79]:

[11] https://eospso.nasa.gov/missions/sentinel-6.

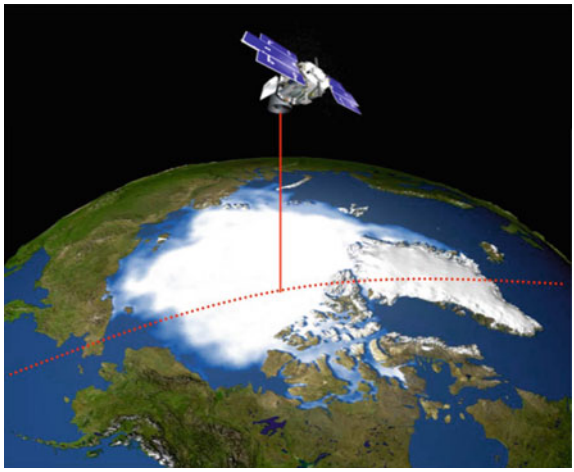

Fig. 9.11 Schematic diagram of ICESat on a transect over the Arctic. ICESat uses a 1064 nm-laser operating at 40 Hz to make measurements at 172-m intervals over ice, oceans, and land. *Source* Abdalati et al. [79]

- Contribute to the development of predictive models that capture both dynamic and surface processes.
- Since the thickness distribution of sea ice controls energy and mass exchanges between the ocean and atmosphere at the surface, and the fresh water fluxes associated with melting ice serve as stabilizing elements in the circulation of the North Atlantic waters, basin-scale fields of ice thickness are therefore essential to improve our estimates of the seasonal and interannual variability in regional mass balance, the freshwater budget of the polar oceans, and the representation of these processes in regional and climate models.
- Its capability of producing a vegetation height surface with 3-m accuracy at 1-km spatial resolution, assuming that off-nadir pointing can be used to increase the spatial distribution of observations over terrestrial surfaces. This sampling, combined with a smaller footprint of 50 m or less, would allow characterization of vegetation at a higher spatial resolution than ICESat, and is expected to provide a new set of global ecosystem applications.
- In addition, the atmospheric measurement capability of ICESat-2, even at near-IR wavelengths, will enable global measurements of cloud and aerosol structure to extend the record of these observations beyond those provided by the current lasers onboard ICESat.

9.5 Concluding Remarks

GNSS remote sensing and its application to environmental monitoring is a new and active area of research. The data that has been collected so far has provided several environmental (atmospheric) properties that were hitherto difficult to fathom. The

new technique clearly promises to contribute significantly to environmental studies. When the life span of the various missions (e.g., GRACE) is reached, thousands of data sets will have been collected that will help to unravel some of the complex nature of atmospheric and environmental phenomenon. From the analysis of water vapour trapped in the atmosphere and tropopause temperature, climate change studies will be significantly enhanced. This will be discussed further in Chaps. 11 and 12.

References

1. Hammond WC, Brooks BA, Bürgmann R, Heaton T, Jackson M, Lowry AR, Anandakrishnan S (2011) Scientific value of real-time Global Positioning System data. Eos 92(15):125–126. doi:10.1029/2011EO150001
2. Yunck TP, Wu SC, Wu JT, Thornton CL (1990) Precise tracking of remote sensing satellites with the global positioning system. IEEE Transactions on Geoscience and Remote Sensing 28:108–116
3. Wickert J (2002) Das CHAMP-Radiookkultationsexperiment: Algorithmen, Prozessierungssystem und erste Ergebnisse. Dissertation. Scientific Technical Report STR02/07, GFZ Potsdam
4. Foelsche U, Borsche M, Steiner AK, Gobiet M, Pirscher B, Kirchengast G, Wickert J, Schmidt T (2008) Observing upper troposphere-lower stratosphere climate with radio occultation from the CHAMP satellite. Climate Dynamics 31:49–65. doi:10.1007/s00382-007-0337-7
5. Schmidt T, Heise S, Wickert J, Beyerle G, Reigber C (2005) GPS radio occultation with CHAMP and SAC-C: global monitoring of thermal tropopause parameters. Atmospheric Chemistry and Physics 5:1473–1488
6. Schmidt T, Wickert J, Beyerle G, Heise S (2008) Global tropopause height trends estimated from GPS radio occultation data. Geophysical Research Letters 35:L11806. doi:10.1029/2008GL034012
7. Seidel DJ, Randel WJ (2006) Variability and trends in the global tropopause estimated from radiosonde data. Journal of Geophysical Research 111:D21101. doi:10.1029/2006JD007363
8. Anthes RA, Bernhardt PA, Chen Y, Cucurull L, Dymond KF, Ector D, Healy SB, Ho SP, Hunt DC, Kuo YH, Liu H, Manning K, McCormick C, Meehan TK, Randel WJ, Rocken C, Schreiner WS, Sokolovskiy SV, Syndergaard S, Thompson DC, Trenberth KE, Wee TK, Yen NL, Zeng Z (2008) The COSMIC/FORMOSAT-3 mission: early results. Bulletin of the American Meteorological Society 89(3):313–333. doi:10.1175/BAMS-89-3-313
9. Bevis M, Businger S, Herring TA, Rocken C, Anthes RA, Ware RH (1992) GPS Meteorology: remote sensing of water vapour using global positioning system. Journal of Geophysical Research 97:15787–15801
10. Hammond WC, Brooks BA, Bürgmann R, Heaton T, Jackson M, Lowry AR, Anandakrishnan S (2010) The scientific value of high-rate, low-latency GPS data, a white paper. http://www.unavco.org/community_science/science_highlights/2010/realtimeGPSWhitePaper2010.pdf. Accessed 06 June 2011
11. Melbourne WG, Davis ES, Duncan CB, Hajj GA, Hardy K, Kursinski R, Mechan TK, Young LE, Yunck TP (1994) The application of spaceborne GPS to atmospheric limb sounding and global change monitoring. JPL Publication 94-18
12. Awange, JL, Fukuda Y, Takemoto S, Wickert J, Aoyama A (2004) Analytic solution of GPS atmospheric sounding refraction angles. Earth, Planet and Space 56: 573–587. doi:10.1186/BF03352518
13. Healey S, Jupp A, Offiler D, Eyre J (2003) The assimilation of radio occultation measurements. In: Reigber C, Lühr H, Schwintzer P (eds) First CHAMP mission results for gravity, magnetic and atmospheric studies. Springer, Heidelberg

14. Kuo Y-H, Sokolovski SV, Anthens RA, Vandenberghe F (2000) Assimilation of the GPS radio occultation data for numerical weather prediction. Terrestrial, Atmospheric and Oceanic Science 11:157–186
15. Steiner AK, Kirchengast G, Foelsche U, Kornblueh L, Manzini E, Bengtsson L (2001) GNSS occultation sounding for climate monitoring. Physics and Chemistry of the Earth (A) 26(3):113–124. doi:10.1016/S1464-1895(01)00034-5
16. Yunck TP (2003) The promise of spaceborne GPS for Earth remote sensing. In: International workshop on GPS meteorology, 14th-17th January 2003, Tsukuba, Japan
17. Anthes RA et al (2004) Application of GPS remote sensing to meteorology and related fields. Journal of Meteorological Society of Japan 82(1B):259–596
18. Foelsche U, Kirchengast G, Steiner AK (2006) Atmosphere and climate. Studies by occultation methods, Springer, Berlin
19. Ware H, Fulker D, Stein S, Anderson D, Avery S, Clerk R, Droegmeier K, Kuettner J, Minster B, Sorooshian S (2000a) SuomiNet: a real-time national GPS network for atmospheric research and education. Bulletin of the American Meteorological Society 81:677–694
20. Ware R (1992) GPS sounding of the earth's atmosphere. GPS World 3:56–57
21. Businger S, Chiswell SR, Bevis M, Duan J, Anthes RA, Rocken C, Ware RH, Exner M, VanHove T, Solheim FS (1996) The promise of GPS in atmospheric monitoring. Bulletin of the American Meteorological Society 77:5–18
22. Ware R, Exner M, Schreiner W, Anthes R, Feng D, Herman B, Gorbunov M, Sokolovskiy S, Hardy K, Kuo Y, Zou X, Trenberth K, Meehan T, Melbourne W, Businger S (1996) GPS sounding of atmosphere from low earth orbit: preliminary results. Bulletin of the American Meteorological Society 77:19–40. doi:10.1175/1520-0477(1996)077<0019:GSOTAF>2.0.CO;2
23. Jin S, Komjathy A (2010) GNSS reflectometry and remote sensing: a new objectives and results. Advances in Space Research 46:111–117
24. Resch GM (1984) Water vapor radiometry in geodetic applications. In: Geodetic Refraction (ed) Brunner FK. Springer, New York, pp 53–84
25. Thayer GD (1974) An improved equation for the radio refractive index of air. Radio Science 9(10):803–807. doi:10.1029/RS009i010p00803
26. Leick A (2004) GPS satellite surveying, 3rd edn. Wiley, New York
27. Davis JL, Herring TA, Shapiro II, Rogers AE, Elgered G (1985) Geodesy by radio interferometry: effects of atmospheric modelling errors on estimates of baseline length. Radio Science 20:1593–1607
28. Niell AE (1996) Global mapping functions for the atmosphere delay at radio wavelengths. Journal of Geophysical Research 101(B2):3227–3246. doi:10.1029/95JB03048
29. Bevis M, Businger S, Chiswell S, Herring TA, Anthes RA, Rocken C, Ware RH (1994) GPS Meteorology: mapping zenith wet delays onto precipitable water. Journal of Applied Meteorology 33:379–386
30. Rocken C, Ware R, Hove TV, Solheim F, Alber C, Johnson J, Bevis M, Businger S (1993) Sensing atmospheric water vapour with the Global Positioning System. Geophysical Research Letters 20(23):2631–2634. doi:10.1029/93GL02935
31. Tralli DM, Lichten SM (1990) Stochastic estimation of tropospheric path delays in global positioning system geodetic measurements. Journal of Geodesy 64:127–159. doi:10.1007/BF02520642
32. Askne J, Nordius H (1987) Estimation of tropospheric delay for microwaves from surface weather data. Radio Science 22:379–386
33. Khandu Awange JL, Wickert J, Schmidt T, Sharifi MA, Heck B, Fleming K (2011) GNSS remote sensing of the Australian tropopause. Climatic Change 105(3–4):597–618. doi:10.1007/s10584-010-9894-6
34. Schmidt T, Wickert J, Beyerle G, Reigber C (2004) Tropical tropopause parameters derived from GPS radio occultation measurements with CHAMP. Journal of Geophysical Research 109:D13105. doi:10.1029/2004JD004566
35. McGrat R, Semmler T, Sweeney C, Wang S (2006) Impact of balloon drift errors in radiosonde data on climate statistics. Journal of climate 19(14):3430–3442. doi:10.1175/JCLI3804.1

36. Wickert J (2004) Comparison of vertical refractivity and temperature profiles from CHAMP with radiosonde measurements. Danish Meteorological Institute, Copenhagen
37. Kuo Y-H, Schreiner WS, Wang J, Rossiter DL, Zhang Y (2005) Comparison of GPS Radio occultation soundings with radiosonde. Geophysical Research Letters 32:L05817. doi:10.1029/2004GL021443
38. Arras C, Jacobi C, Wickert J, Heise S, Schmidt T (2010) Sporadic E signatures revealed from multi-satellite radio occultation measurements. Advances in Radio Science 8:225–230. doi:10.5194/ars-8-225-2010
39. Wickert J, Beyerle G, Hajj GA, Schwieger V, Reigber C (2002) GPS radio occultation with CHAMP: atmospheric profiling utilizing the space-based single differencing technique. Geophysical Research Letters 29(8):1187. doi:10.1029/2001GL013982
40. Beyerle G, Schmidt T, Michalak G, Heise S, Wickert J, Reigber C (2005) GPS radio occultation with GRACE: atmospheric profiling utilizing the zero difference technique. Geophysical Research Letters 32(L13806): doi:10.1029/2005GL023109
41. Wickert J, Michalak G, Schmidt T, Beyerle G, Cheng C, Healy S, Heise S, Huang C, Jakowski N, Köhler W, Mayer C, Offiler D, Ozawa E, Pavelyev A, Rothacher M, Tapley B, Arras C (2009) GPS radio occultation: results from CHAMP, GRACE and FORMOSAT-3/COSMIC. Terrestrial, Atmospheric and Oceanic Sciences 20:35–50. doi:10.3319/TAO.2007.12.26.01(F3C)
42. Cheng CZ, Kuo Y-H, Anthes RA, Wu L (2006) Satellite constellation monitors global and space weather. EOS, Transactions American Geophysical Union 87(17):166. doi:10.1029/2006EO170003
43. Tsuda T, Hocke K (2004) Application of GPS occultation for studies of atmospheric waves in the Middle Atmosphere and Ionosphere. In: Anthens et al (eds) Application of GPS remote sensing to meteorology and related fields. Journal of Meteorological Society of Japan, vol 82, No. 1B, pp 419–426
44. Chen G, Herring TA (1997) Effects of atmospheric azimuthal asymmetry on the analysis of apace geodetic data. Journal of Geophysical Research 102(B9):20489–20502
45. Tsuda T, Heki K, Miyazaki S, Aonashi K, Hirahara K, Tobita M, Kimata F, Tabei T, Matsushima T, Kimura F, Satomura M, Kato T, Naito I (1998) GPS meteorology project of Japan - Exploring frontiers of geodesy - Earth Planets Space, 50(10): i–v
46. Hanssen RF, Weckwerth TM, Zebker HA, Klees R (1999) High-Resolution water vapor mapping from interferometric radar measurements. Science 283:1297–1299. doi:10.1126/science.283.5406.1297
47. Heise S, Wickert J, Beyerle G, Schmidt T, Reigber C (2006) Global monitoring of tropospheric water vapor with GPS radio occultation aboard CHAMP. Advances in Space Research 37(12):2222–2227. doi:10.1016/j.asr.2005.06.066
48. Tregoning P, Watson C, Ramillien G, McQueen H, Zhang J (2009) Detecting hydrologic deformation using GRACE and GPS. Geophysical Research Letters 36:L15401. doi:10.1029/2009GL038718
49. Hirt C, Gruber T, Featherstone WE (2011) Evaluation of the first GOCE static gravity field models using terrestrial gravity, vertical deflections and EGM2008. quasigeoid heights. Journal of Geodesy 85:723–740. doi:10.1007/s00190-011-0482-y
50. Rieser D (2008) Comparison of GRACE-derived monthly Surface Mass Variations with Rainfall Data in Australia. MSc thesis. Graz University of Technology
51. Pool DR, Eychaner JH (1995) Measurements of aquifer-storage change and specific yield using gravity surveys. Groundwater 33(3):425–432. doi:10.1111/j.1745-6584.1995.tb00299.x
52. Ellett KM, Walker JP, Western AW, Rodell M (2006) A framework for assessing the potential of remote sensed gravity to provide new insight on the hydrology of the Murray–Darling Basin. Australian Journal of Water Resources 10(2):89–101
53. Awange JL, Sharifi MA, Baur O, Keller W, Featherstone WE, Kuhn M (2009) GRACE hydrological monitoring of Australia. Current limitations and future prospects. Journal of Spatial Science 54(1):23–36. doi:10.1080/14498596.2009.9635164
54. Rummel R, Balmino G, Johannessen J, Visser P, Woodworth P (2002) Dedicated gravity field missions - principles and aims. Journal of Geodynamics 33(1):3–20. doi:10.1016/S0264-3707(01)00050-3

55. Schrama EJO, Visser PNAM (2007) Accuracy assessment of the monthly GRACE geoids based upon a simulation. Journal of Geodesy 81(1):67–80. doi:10.1007/s00190-006-0085-1
56. Prasad R, Ruggieri M (2005) Applied satellite navigation using GPS. GALILEO and augmentation systems, Artech House, Boston/London
57. Luthcke S, Rowlands D, Lemoine F, Klosko S, Chinn D, McCarthy J (2006) Monthly spherical harmonic gravity field solutions determined from GRACE inter-satellite range-rate data alone. Geophysical Research Letters 33:L02402. doi:10.1029/2005GL024846
58. Tapley BD, Bettadpur S, Ries JC, Thompson PF, Watkins MM (2004) GRACE measurements of mass variability in the Earth system. Science 305:503–505. doi:10.1126/science.1099192
59. Bruinsma S, Lemoine J, Biancale R, Valès N (2010) CNES/GRGS 10-day gravity field models (release 2) and their evaluation. Advances in Space Research 45(4):587–601. doi:10.1016/j.asr.2009.10.012
60. Lemoine F, Luthcke S, Rowlands D, Chinn D, Klosko S, Cox C (2007) The use of mascons to resolve time-variable gravity from GRACE. In: Tregoning P, Rizos C (eds) Dynamic planet. Springer, Berlin, pp 231–236
61. Ramillien G, Cazenave A, Brunau O (2004) Global time variations of hydrological signals from GRACE satellite gravimetry. Geophysical Journal International 158(3):813–826. doi:10.1111/j.1365-246X.2004.02328.x
62. Chambers D, Wahr J, Nerem R (2004) Preliminary observations of global ocean mass variations with GRACE. Geophysical Research Letters 31(L13310): doi:10.1029/2004GL020461
63. Wahr J, Jayne S, Bryan F (2002) A method of inferring changes in deep ocean currents from satellite measurements of time-variable gravity. Journal of Geophysical Research 107(C12):3218. doi:10.1029/2002JC001274
64. Rodell M, Famiglietti JS (1999) Detectability of variations in continental water storage from satellite observations of the time dependent gravity field. Water Resources Research 35(9):2705–2724. doi:10.1029/1999WR900141
65. Tiwari V, Wahr J, Swenson S (2009) Dwindling groundwater resources in northern India, from satellite gravity observations. Geophysical Research Letters 36:L18401. doi:10.1029/2009GL039401
66. Werth S, Güntner A, Petrovic S, Schmidt R (2009) Integration of GRACE mass variations into a global hydrological model. Earth and Planetary Science Letters 27(1–2):166–173. doi:10.1016/j.epsl.2008.10.021
67. Baur O, Kuhn M, Featherstone W (2009) GRACE-derived ice-mass variations over Greenland by acocunting for leakage effects. Journal of Geophysical Research 114(B06407). doi:10.1029/2008JB006239
68. Velicogna I (2009) Increasing rates of ice mass loss from the Greenland and Antarctic ice sheets revealed by GRACE. Geophysical Research Letters 36:L19503. doi:10.1029/2009GL040222
69. Boy J-P, Chao B (2005) Precise evaluation of atmospheric loading effects on Earth's time-variable gravity field. Journal of Geophysical Research 110:B08412. doi:10.1029/2002JB002333
70. Swenson S, Wahr J (2002) Estimated effects of the vertical structure of atmospheric mass on the time-variable geoid. Journal of Geophysical Research 107(B9):2194. doi:10.1029/2000JB000024
71. Barletta V, Sabadini R, Bordoni A (2008) Isolating the PGR signal in the GRACE data: impact on mass balance estimates in Antarctica and Greenland. Geophysical Journal International 172(1):18–30. doi:10.1111/j.1365-246X.2007.03630.x
72. Tregoning P, Ramillien G, McQueen H, Zwartz D (2009) Glacial isostatic adjustment and nonstationary signals observed by GRACE. Journal of Geophysical Research 114:B06406. doi:10.1029/2008JB006161
73. Swenson S, Wahr J, Milly PCD (2003) Estimated accuracies of regional water storage variations inferred from the Gravity Recovery and Climate Experiment (GRACE). Water Resources Research 39(8):1223. doi:10.1029/2002WR001736
74. Ramillien G, Frappart F, Cazenave A, Gutner A (2005) Time variations of land water storage from an inversion of two years of GRACE geoids [rapid communication]. Earth and Planetary Science Letters 235(1–2):283–301. doi:10.1016/j.epsl.2005.04.005

75. Wahr J, Molenaar M, Bryan F (1998) Time variability of the Earth's gravity field: hydrological and oceanic effects and their possible detection using GRACE. Journal of Geophysical Research (Solid Earth) 103(B12):30205–30230. doi:10.1029/98JB02844
76. Heiskanen WA, Moritz H (1967) Physical geodesy. W.H, Freeman and Company, San Francisco
77. Yang Q (2016) Applications of Satellite Geodesy in Environmental and Climate Change. Graduate Theses and Dissertations. http://scholarcommons.usf.edu/etd/6440. Accessed 26 Jan 2017
78. Pugh D (2004) Changing sea levels. Effect of tides, weather and climate. Cambridge Univeristy Press
79. Abdalati W, Zwally HJ, Bindschadler B, Csatho B, Farrell SL, Fricker HA, Harding D, Kwok R, Lefsky M, Markus T, Marshak A, Neumann T, Palm S, Schutz B, Smith B, Spinhirne J, Webb C (2010) The ICESat-2 laser altimetry mission. Proceedings of the IEEE 98(5):735–751. doi:10.1109/JPROC.2009.2034765